The achievement of fuel gain exceeding unity in an inertially confined fusion implosion

O. A. Hurricane, D. A. Callahan, D. T. Casey, P. M. Celliers, C. Cerjan, E. L. Dewald, T. R. Dittrich, T. Doppner, D. E. Hinkel, L. F. Berzak Hopkins, J. L. Kline, S. Le Pape, T. Ma, A. G. MacPhee, J. L. Milovich, A. Pak, H. S. Park, P. K. Patel, B. A. Remington, J. D. Salmonson, P. T. Springer, R. Tommasini

October 28, 2013

Nature

Disclaimer

This document was prepared as an account of work sponsored by an agency of the United States government. Neither the United States government nor Lawrence Livermore National Security, LLC, nor any of their employees makes any warranty, expressed or implied, or assumes any legal liability or responsibility for the accuracy, completeness, or usefulness of any information, apparatus, product, or process disclosed, or represents that its use would not infringe privately owned rights. Reference herein to any specific commercial product, process, or service by trade name, trademark, manufacturer, or otherwise does not necessarily constitute or imply its endorsement, recommendation, or favoring by the United States government or Lawrence Livermore National Security, LLC. The views and opinions of authors expressed herein do not necessarily state or reflect those of the United States government or Lawrence Livermore National Security, LLC, and shall not be used for advertising or product endorsement purposes.

The achievement of fuel gain exceeding unity in an inertially confined fusion implosion

O.A. Hurricane[1], D.A. Callahan[1], D.T. Casey[1], P.M. Celliers[1], C. Cerjan[1], E.L. Dewald[1], T.R. Dittrich[1], T. Döppner[1], D.E. Hinkel[1], L.F. Berzak Hopkins[1], J.L. Kline[2], S. LePape[1], T. Ma[1], A.G. MacPhee[1], J.L. Milovich[1], A. Pak[1], H.-S. Park[1], P.K. Patel[1], B.A. Remington[1], J.D. Salmonson[1], P.T. Springer [1], & R. Tommasini[1]

[1]*Lawrence Livermore National Laboratory, P.O. Box 808, Livermore, California 94551, USA*

[2]*Los Alamos National Laboratory, Los Alamos, New Mexico 87545, USA*

Ignition has been a long sought-after goal needed to make fusion energy a viable alternative energy source, but has yet to be achieved.[1] A key step on the way to ignition is to have the energy generated through fusion reactions in an inertially confined fusion (ICF) plasma exceed the amount of energy deposited into the deuterium-tritium (DT) fusion fuel and hot-spot during the implosion process for a fuel gain, G_{fuel}, exceeding unity. Using the implosion developed by our team,[2,3] fusion fuel gains exceeding unity have been achieved on the National Ignition Facility (NIF) and the results are reported on herein. These experiments on the NIF show an order of magnitude improvement in yield performance over past shots. We are also seeing a significant contribution to the yield coming from alpha-particle self-heating and evidence for the "bootstrapping" required to accelerate the DT fusion burn-rate to eventually run-away ignite.

At the NIF, 192 lasers deliver up to 1.8 MJ of light into a gold hohlraum (Fig. 1) that converts

the energy into a nearly Planckian x-ray bath. A fraction of the x-rays are absorbed by a capsule generating ~ 100 Mbar pressure in the ablator. This ablation pressure, delivered as a series of weak shocks, accelerates the capsule inwards. Against the inside of the ablator is the DT fuel shell, that is initially in a cryogenic ice state. When the implosion achieves peak velocity, the fuel has a kinetic energy that is a fraction of the x-ray energy absorbed by the capsule. As the fuel stagnates at the center of the implosion, the DT forms a hot-spot from the fuel's inner surface and pdV work is done on the hot-spot. The hot-spot initiates the fusion reactions, producing neutrons and alpha-particles as the hot-spot ion temperature climbs to many keV. At sufficient hot-spot areal density, $(\rho r)_{hs} > 0.3$ g/cm^2 and ion temperature, $T_{ion} > 4$ keV, the hot-spot will "ignite" as alpha-particles redeposit their energy locally. If $(\rho r)_{fuel} > 1$ g/cm^2 the burn will propagate and a runaway self-heating process releases energy many times greater than that absorbed by the capsule.

Mix can both degrade the ability of an ICF implosion to compress the DT fuel and can also cause undesirable cooling as high-Z materials in the DT hot-spot will rapidly radiate away energy in the form of bremsstrahlung emission, the power of emission scaling as $\sim Z^2$ (Z being the atomic number). Among many motivations, the high-foot implosion[2,3] was developed in the wake of the National Ignition Campaign (NIC)[4,5] to primarily address the possibility that ablation front driven instability[6,7] was responsible for part of the observed degraded yield performance[1] and ablator-fuel mix inferred from x-ray emissions in combination with primary neutron yield.[8,9]

The high-foot implosion is designed to reduced ablation-front instability growth and thereby inhibit CH ablator from mixing into and contaminating the DT hot-spot. The laser pulse-shape

is designed to obtain a relatively high hohlraum radiation temperature ($T_{rad} \sim 90 - 100$ eV)

during the "foot" of the pulse (see Fig. 1) and launches 3 shocks. In contrast, the NIC implosion

pulse-shape drives a lower radiation temperature ($T_{rad} \sim 60$ eV) in the foot (hence "low-foot")

for a longer time duration and launches 4 shocks. The essential stability benefits of the high-foot

scheme can be understood from examining an expression for the linear growth-rate of ablation

driven Rayleigh-Taylor (RT) instability[10]

$$\gamma_{A-RTI} = \alpha_2(Fr, \nu)\sqrt{\frac{kg}{1 + kL_\rho}} - \beta_2(Fr, \nu)kv_a \qquad (1)$$

where k is the perturbation wavenumber, g is the ablator acceleration, L_ρ is the density gradient

scale-length of the ablation front, v_a is the ablation velocity, and α_2 and β_2 are parameters of order

unity whose exact values depend upon a heat conduction scale-length parameter, ν, and the Froude

number, $Fr = v_a^2/(gL_\rho)$. The key stabilizing effects of the high-foot drive enter through the

higher ablation velocity which scales as $T_{rad}^{9/10}$ increasing the $\beta_2 kv_a$ ablative stabilization term of

Eq. (1) and through an increase in L_ρ which reduces the $\sqrt{kg}$ unstable RT drive term. The increase

in L_ρ is primarily due to a stronger 1st shock which increases the adiabat of the implosion and

prevents the ablator from becoming so highly compressed (risking break-up) during the implosion.

The enhanced stability can be further understood by comparing the in-flight-aspect ratio's (IFAR),

$R_{in}/\Delta R$, where R_{in} is the ablator inner radius and ΔR is the ablator thickness: for the high-foot

implosion the IFAR is roughly half of that of the low-foot implosion – the amplitude of instability

growth is directly related to the exponent of $\sqrt{R_{in}/\Delta R}/2$.[11] The trade-off made to obtain the

improved stability of the high-foot is that the DT fuel adiabat, $a = P/P_F$ (usually denoted as α,

but denoted here as a to avoid confusion with α_2 above or α-particles; P is pressure and P_F is

the Fermi pressure – also note an alternate definition of adiabat using P_{cold} is sometimes used[12]), is higher, making the fuel less compressible for a given amount of absorbed energy. Details on the stability benefits, other theoretical motivations, and trade-offs for the high-foot, and the initial results from the first set of five DT implosion experiments are described in a two companion letters[2,3].

DT implosions, N130927 and N131119 (NIF shot number in year-month-day format YYM-MDD) built upon the previous high-foot shot, N130812,[3] by modestly increasing the NIF laser power/energy (Table I) and by redistributing energy between different laser beams, through laser light wavelength changes that affect the cross-beam-transfer (the transfer of power from one beam to another via induced Brillouin scattering), to optimize the illumination pattern in the hohlraum.[13–16] While some simulation capability exists[17] to predict the hot-spot shape changes that result from these wavelength changes, in practice the precise wavelengths needed to tune in the desired (i.e. round) shape are found empirically. For N130927, the choice of $\lambda_{23.5} - \lambda_{30} = 0.7$Å between the 23.5° and 30.0° inner cone beams was chosen for azimuthal symmetry control with $\Delta\lambda_{23.5-outer} = 9.2$ Å and $\Delta\lambda_{30-outer} = 8.5$ Å used for equatorial symmetry control (see Fig. 1 for beam angles). For N131119, $\Delta\lambda_{23.5-outer} = 9.5$ Å and $\Delta\lambda_{30-outer} = 8.8$ Å . These wavelength choices were critical for keeping the hot-spot shape in-check as the implosion was pushed to higher velocities as previous experiments had already shown the tendency towards oblate toroidal hot-spots when laser power was increased[3]. There are limits to the amount of control that can be exerted over the hot-spot shape just through wavelength changes alone and that physical changes to the hohlraum may also be required in future experiments to maintain an acceptable hot-spot (and fuel) shape to

achieve the desired results.

We used a gold hohlraum of 5.75 mm diameter and 9.425 mm length as was typical of most high-foot cryogenic DT implosion experiments (see Fig. 1). The same hohlraum geometry was used during the NIC for most of the low-foot shots. As is typical for the high-foot series, the hohlraum is filled with helium gas of 1.6 mg/cc density (as compared to 0.96 mg/cc for the NIC) the purpose of which is to restrict and delay gold plasma from blowing in from the inside wall of the hohlraum which can otherwise impede laser beam propagation. The CH plastic capsule at the center of the hohlraum for N130927 (N131119) had a 1.1315 (1.1241) mm outer shell radius and 0.9365 (0.9303) mm inner shell radius (see Fig. 1). Layered on the inner surface of the capsule shell for N130927 (N131119) was 71.4 (69.3) μm of cryogenic DT ice that was held at 0.8 K below the triple-point for a shot temperature of 18.6 K, like all high-foot DT shots—a so-called mini-quench condition that generally produces an ice layer with fewer ice cracks than that of a full quench.[18] Characterization of the capsule surface showed roughness typical of implosion capsules for NIF while characterization of the DT ice showed roughness well within requirements. The very high quality of the DT ice layer on N130927 was likely not a significant factor in its performance since the third highest performing shot on NIF (N130812) had an ice layer that was somewhat worse than average. The DT layer quality for N131119 was in between the quality of the layers of N130812 and N130927.

Table I shows the key measurements and performance metrics for NIF shots N130927 and N131119. Key measured quantities are neutron yield, Y_{13-15}, in the 13-15 MeV energy band

5

around the characteristic 14.1 MeV DT fusion neutron energy, burn averaged ion-temperature (T_{ion}), neutron and x-ray burn-widths (τ_n and τ_x), down-scatter-ratio (DSR), and the time of peak neutron brightness ("bang-time", t_b). On the NIF, Y_{13-15} is an average of many diagnostics including four neutron time-of-flight (NToF) detectors[19], numerous radiochemical activation measurements[20], and a magnetic recoil spectrometer (MRS) [21]. T_{ion} is directly related to the temporal spread obtained from the full-width-half-max (FWHM) of the NToF detectors. A temporal gamma ray history gives τ_n (for the high-foot experiments τ_x and τ_n are consistent to within error bars). The DSR comes from measuring, via NToF and MRS, the number of neutrons scattered into the energy range 10-12 MeV and is directly related to the areal density of the cold DT fuel, $(\rho r)_{fuel} \approx 20.3 \cdot f \cdot DSR$ (where f depends upon the amount of ablator mass remaining but is typically 0.95 ± 0.05.[21,22] Other diagnostics such as x-ray imaging and neutron imaging (Fig. 2) give information on the shape of the implosion.

In what follows, we will use the aforementioned observables that are measured over the duration of the fusion burn to infer the amount of energy that was deposited into the DT (both fuel and hot-spot) in order to compare to the amount of energy generated from fusion. The details of the analysis will focus upon N130927, while the numbers for N131119, that exceeded the performance of N130927, are just quoted in Table I. The analysis outlined in this letter follows an essentially 1D onion-skin picture with a uniform density and temperature hot-spot surrounded by the fuel (with Gaussian or uniform density profile in radius), albeit the observed 3D hot-spot shape information is used to obtain the hot-spot volume. Also an assumption of equal ion and electron temperatures, $T_{ion} \approx T_e$ is made and can be justified *post hoc* using an expression for the electron-

ion collision time after the hot-spot density is obtained. Results from analysis and simulation with less simplified assumptions are also quoted in Table I for comparison to what is detailed below.

Analyzing the observed hot-spot shape (Fig. 2) in terms of Legendre modes (equatorial view, lines 6-9 of Table I) and Fourier modes (polar view), where the hot-spot perimeter, as defined by the 17% of peak brightness contour, is given by

$$R_{hs}(\theta) = P0 \left[1 + \sum_{\ell=2}^{\infty} \left(\frac{P\ell}{P0} \right) P_{\ell}(\cos\theta) \right], \tag{2}$$

one can obtain the hot-spot volume V_{hs} (see Methods section) and effective spherical radius $r_{hs} = [3V_{hs}/(4\pi)]^{(1/3)}$. (Note that there is no absolute reference for the x-ray or neutron images so mode $\ell = 1$ is not included in the shape description, however $\ell = 1$ and $m = 1$ motions can be obtained from the NToF detectors). The total neutron yield, Y_{total}, can be calculated from $Y_{total} = Y_{13-15} \cdot \exp(4 \cdot DSR)$ which accounts for the neutrons produced but then scattered by the cold and dense DT fuel out of the measured 13-15 MeV energy band. Since for DT fusion reactions the energy per fusion is known (14.1 MeV per neutron and 3.5 MeV per alpha-particle), E_{fusion}, the total fusion energy produced, can be calculated from Y_{total}.

From the measured T_{ion} the DT reaction-rate per unit volume, $\langle \sigma v \rangle$, can be calculated with standard formulae[23] (see Methods section). For N130927, $\langle \sigma v \rangle = 4.75 \times 10^{-18}$ - 1.03×10^{-17} cm^3/s The range of values is driven by the differences in T_{ion} coming from DT vs. DD NToF interpretation. The reported T_{ion} values are actually averages over several detectors. The observed spread in the individual detector T_{ion} interpretations indicates some motional broadening contribution, which suggests that the lower temperature is more representative of the thermal temperature.

7

Throughout this letter, the uncertainty ranges given for values for all quoted quantities are driven by the uncertainty in T_{ion}.

For a 50-50 DT mix then the fusion power density is $\dot{\epsilon}_{DT} = 7.04 \times 10^{-13} n^2 \langle \sigma v \rangle$ in J/(cm^3·s), where n is the yet unknown number density of the fusing region. With E_{fusion}, V_{hs}, and τ_x the hot-spot number density can be calculated

$$n = \sqrt{\frac{E_{fusion}}{7.04 \times 10^{-13} \langle \sigma v \rangle V_{hs} \tau_x}}. \tag{3}$$

For N130927, $n = 8.1 \times 10^{24}$ - 1.2×10^{25} cm^{-3} a value that also then provides the hot-spot mass density (assuming a pure DT hot-spot, average atomic number $\bar{A} = 2.5$ for DT), $\rho_{hs} = 34$ - 50 g/cc, hot-spot mass, $m_{hs} = \rho_{hs} V_{hs} = 6.4$ - 9.4 μg, and areal density, $(\rho r)_{hs}$ found in Table I.

A number of quantities describing the implosion energetics now straightforwardly follow. The hot-spot pressure can be obtained from $P_{hs} = (\bar{Z} + 1)\rho_{hs} T_{ion}/\bar{A}$ ($\bar{Z} = 1$ for DT) to find $P_{hs} = 126$ - 152 Gbar. The hot-spot energy is then $E_{hs} = \frac{3}{2} P_{hs} V_{hs}$ (Table I). The fraction, f_α, of alpha-particle energy deposited into the hot-spot can be calculated from a classic formula[24]

$$f_\alpha = 1 - \frac{1}{4[(\rho r)_{hs}/\rho \lambda_\alpha]} + \frac{1}{160[(\rho r)_{hs}/\rho \lambda_\alpha]^3} \tag{4}$$

where the α-particle stopping range can be found from[25]

$$\rho \lambda_\alpha = \frac{0.025 T_e^{5/4}}{1 + 0.0082 T_e^{5/4}} \tag{5}$$

in cm, g, keV units. For N130927, $f_\alpha = 0.68$ - 0.82. The energy deposited in the hot-spot by alpha-particles is $E_\alpha = f_\alpha E_{fusion}/5$ recalling that 1/5 of the DT fusion energy is emitted in the

form of α-particles (the remaining α-particle energy is deposited into the cold fuel). Note that, using the values found in Table I, $E_\alpha/E_{hs} \approx 0.56$. These energies fully describe the hot-spot, but part of the implosion energy was used to compress the remaining cold DT fuel so we must examine the fuel in order to get a full picture of the implosion energy balance.

Since the DT hot-spot is formed by ablating the inner surface of the cold DT fuel as electron conduction transports heat from the forming hot-spot into the fuel, we can calculate the amount of DT fuel remaining after the hot-spot has formed knowing the initial amount of DT ice layered onto the inside of the capsule, $m_0 = 186$ μg (for N130927), so $m_{fuel} = m_0 - m_{hs} = 176$ - 179 μg. The cold DT fuel mass forms a shell surrounding the hot-spot with volume $V_{fuel} = \frac{4\pi}{3}(r_{out}^3 - r_{hs}^3)$, where r_{out} is the unknown outer fuel radius. Since $m_{fuel} = 4\pi \int \rho_{fuel} r^2 dr$ and the measured DSR provides a way to obtain the fuel density, ρ_{fuel}, from $(\rho r)_{fuel} = \int \rho_{fuel} dr$, assuming a fuel profile, we can solve for both the fuel layer thickness, $r_{out} - r_{hs}$, and density ρ_{fuel} (see Methods section)

$$r_{out} - r_{hs} = 2\sigma = \sqrt{\frac{m_{fuel}}{2\pi(\rho r)_{fuel}} - r_{hs}^2} - r_{hs} \tag{6}$$

with a Gaussian density profile, $\rho(r) = (\rho r)_{fuel} \exp[-(r - r_0)^2/(2\sigma^2)]/(\sqrt{2\pi}\sigma)$, r_0 being the radius of peak fuel density. For N130927, $r_{out} - r_{hs} = 14.7$ - 15.3 μm, $\rho_{fuel} = 385$ - 402 g/cc, $V_{fuel} = (3.0$ - $3.2) \times 10^5$ μm^3. The fuel outer radius from these arguments, $r_{out} = 50.8$ μm (at 50% ρ_{fuel}), is close to that obtained directly from the down-scattered neutron image (Fig. 2), where $P0 = 55.4$ μm (at 17% max. intensity). By this time of peak compression the DT fuel density has increased a factor of $> 1500\times$. The fuel density is not required for calculating the fuel energy, but it can be used to estimate the adiabat of the fuel (at bang-time) assuming that the cold fuel and hot-spot are isobaric ($P_{fuel} \approx P_{hs}$) in which case we find $a = P_{fuel}/P_{Fermi} \approx$

9

$P_{hs}/(0.0021\rho_{fuel}^{5/3}) = 2.9 - 3.3$ for N130927 – the fuel adiabat in-flight is lower than this range of values. The fuel density is also needed to calculate the x-ray losses through the fuel.

As the hot-spot is compressed to high temperatures, the primary energy loss mechanism is Bremsstrahlung x-ray emission since the DT hot-spot is optically thin to these x-rays. Expressions for Bremsstrahlung energy loss can be obtained from many physics texts[25] and calculated (in cm, keV, s units)

$$E_{Brems}(kJ) = 5.34 \times 10^{-34} n_{hs}^2 \sqrt{T_e} V_{hs} \tau_x. \tag{7}$$

For N130927, $E_{brems} = 2.3$ - 4.5 kJ the low end of which is nearly equivalent to the alpha-particle energy deposited. To examine whether or not these x-rays can escape the dense cold fuel, we can calculate the optical depth of the cold DT fuel from $\tau_{fuel} = \rho_{fuel}\kappa_{DT}(r_{out} - r_{hs})$ using a simple DT opacity model, κ_{DT} (g/cm^2) $= 0.352\rho_{fuel}(h\nu)^{-3.3}[1 - \exp(-h\nu/T_e)]$ to find that for x-ray energies $h\nu \sim T_{ion} \sim T_e$ the DT fuel layer is almost one optical depth, $\tau_{fuel} = 0.32 - 0.66$, so some Bremsstrahlung x-rays deposit energy into the cold fuel while some escape. Electron conduction does not play a significant role in the total DT energy loss from the cold fuel at stagnation, but is important for the hot-spot energy loss.

The cold fuel energy at stagnation now follows from the isobaric assumption, $E_{fuel} = \frac{3}{2}P_{fuel}V_{fuel} = 6.9$ - 7.8 kJ (here we've over-estimated the fuel internal energy since typically the outer edge of the fuel has not fully stagnated even at bang-time). The total energy delivered to the DT by the implosion is then (see Table I)

$$E_{DT,total} = E_{hs} + E_{fuel} + \frac{1}{2}e^{-\tau_{fuel}}E_{Brems} - \frac{1}{2}E_\alpha. \tag{8}$$

10

The factor of $\frac{1}{2}$ on the radiation term and alpha-particle energy deposition accounts for having only half the energy emitted or deposited at peak burn. This total DT energy was calculated with quantities measured around bang-time, but this energy represents the kinetic plus internal energy in the fuel at peak velocity in the implosion. A cross-check of $E_{DT,total}$ is provided from calculating the fuel kinetic energy, K, using a direct measurement of implosion velocity from an earlier high-foot "1DConA" shot N130409 (at 350 TW and 1.3 MJ of laser power and energy), where the peak ablator center-of-mass velocity was measured to be 267 ± 15 km/s being equivalent to a fuel velocity of 297 ± 15 km/s (the fuel being at smaller radius and convergence make velocity larger). Scaling the N130409 derived velocity to the laser power of N130927 ($v_{imp} \sim P_{laser}^{0.41}$) gives a fuel velocity of $v_{fuel} = 311 \pm 15$ km/s, so $K = \frac{1}{2}m_0 v_{fuel}^2 = 9.0 \pm 0.9$ kJ. The difference between K and $E_{DT,total}$ is the internal energy in the fuel at peak velocity plus additional pdV work done by the ablator on the fuel during the deceleration.

The total fuel energy gain, $G_{fuel} = E_{fusion}/E_{DT,total}$ is now known and is 1.2-1.4 for N130927. For comparison also shown in Table I are results from other data derived models of implosion energetics[26,27] that are constructed in the same spirit of the above analysis but that differ in some details. A conduction limited temperature profile in the hotspot is added to the above development in one case[26] and the other "detailed model" case includes a 3D self-consistent physics model matched to the data.[27] To complement these analytic data driven models, Table I also shows the results from a full physics radiation-hydrodynamics 1D simulation[28] of N130927, with a multi-frequency x-ray drive that is calibrated to shock-timing and implosion trajectory data, without any mix model applied. The inferences from data and the computer simulation all indicate $G_{fuel} > 1$

– the first time ever achieved in controlled fusion research. Moreover, we have demonstrated re-peatability and improvement with the follow-on shot N131119. It should be understood however that $G_{fuel} > 1$ while a scientific milestone with the fusion energy out exceeding the energy de-posited into the *fuel* is not the same as exceeding the energy absorbed by the *capsule* (defined as the ablator shell plus DT fuel) which absorbed ~ 150 kJ for N130927 and N131119 nor the energy delivered by the laser to the *target* (defined as the hohlraum plus capsule) which was 1.8 MJ and 1.9 MJ respectively for N130927 and N131119.

Key yield and energy performance metrics are graphically illustrated in Figure 3 for N131119, N130927, and all other DT implosions carried out on the NIF since the summer of 2011. Using a key metric for ignition, the generalized Lawson criteria (GLC) $\chi = (P\tau)/(P\tau)_{ign}$ (which is unity at ignition)[29] we see (Figure 3 inset) that for N131119 we are at the threshold of achieving a yield doubling due to alpha-particle energy deposition.

Since most ICF quantities that we seek to improve to get closer to ignition scale as some pos-itive power of stagnation pressure, near term efforts focus upon increasing the implosion speed and controlling the hot-spot shape with the present fuel adiabat. As the implosion speed is increased we will necessarily risk the possibility of giving back some of the gains the high-foot implosion has made in terms of instability control. New strategies for the hohlraum will also be explored since presently hohlraum physics is limiting our ability to use the full power capability of the NIF while also maintaining an acceptable hot-spot shape (higher laser powers are the most direct way to increase implosion speed). Future efforts may involve more elaborate schemes to keep the ablator

instability control while recovering a lower adiabat for the fuel (e.g. "adiabat shaping")[30] or using an alternate ablator material as well.

METHODS SUMMARY

Formulea for the hot-spot volume, DT reaction-rate, and a discussion of fuel density profiles are given in the Full Methods. Neutron image shape coefficients are also given.

1. Edwards, M. J. *et al.* Progress towards ignition on the National Ignition Facility. *Phys Plasmas*, **20**, 070501 (2013).

2. Dittrich, T. R. *et al.* Design of a High-foot/High-Adiabat ICF Capsule for the National Ignition Facility. *Phys. Rev. Lett., in print* (2013).

3. Park, H.-S. *et al.* High-Adiabat, high-foot, inertial confinement fusion implosion experiments on the National Ignition Facility. *Phys. Rev. Lett., in print* (2013).

4. Lindl, J. D. & Moses, E. I. Plans for the National Ignition Campaign (NIC) on the National Ignition Facility (NIF): On the threshold of initiating ignition experiments. *Phys. Plasmas*, **18**, 050901 (2011).

5. Glenzer, S. H. *et al.* Cryogenic thermonuclear fuel implosions on the National Ignition Facility, *Phys. Plasmas*, **19**, 056318 (2012).

6. Bodner, S. E. Rayleigh-Taylor instability and laser-pellet fusion, *Phys. Rev. Lett.*, **33**, 761-764 (1974).

7. Gonchorov, V. N. & Hurricane, O. A. *Panel 3 Report: Implosion Hydrodynamics* (LLNL Report LLNL-TR-562104, 2012). *Op cit. Science of Fusion Ignition on NIF Workshop May 22-24, 2012* (LLNL Report LLNL-TR-570412, 2012).

8. Ma, T. *et al.* Onset of Hydrodynamic Mix in High-Velocity, Highly Compressed Inertial Confinement Fusion Implosions. *Phys. Rev. Lett.*, **111**, 085004 (2013).

9. Regan, S. P. *et al.* Hot-spot Mix in Ignition-scale Inertial Confinement Fusion Targets. *Phys. Rev. Lett.*, **111**, 045001 (2013).

10. Betti, R., Goncharov, V. N., McCrory, R. L. & Verdon, C. P., Growth rates of the Rayleigh-Taylor instability in inertial confinement fusion. *Phys. Plasmas*, **5** 1446-1454 (1998).

11. Lindl, J. Development of the indirect-drive approach to inertial confinement fusion and the target physics basis for ignition and gain, *Physics of Plasmas*, **2**, 3933-4024 (1995).

12. Haan, S. *et al.* Point design targets, specifications, and requirements for the 2010 ignition campaign on the National Ignition Facility. *Phys. Plasmas*, **18**, 051001 (2011).

13. Michel, P. *et al.* Tuning the Implosion Symmetry of ICF Targets via Controlled Crossed-Beam Energy Transfer. *Phys. Rev. Lett.*, **102**, 025004 (2009).

14. Michel, P. *et al.* Symmetry tuning via controlled crossed-beam energy transfer on the National Ignition Facility. *Phys. Plasmas*, **17**, 056305 (2010).

15. Moody, J. D. *et al.* Multistep redirection by cross-beam power transfer of ultrahigh-power lasers in a plasma. *Nature Physics*, **8**, 344-349 (2012).

16. Callahan, D. A. *et al.* The velocity campaign for ignition on NIF. *Phys. Plasmas*, **19**, 056305 (2012).

17. Marinak, M. M. *et al.* Three-dimensional HYDRA simulations of National Ignition Facility targets. *Phys. Plasmas*, **8**, 2275 (2001).

18. Kozioziemski, B. J. *et al.* Deuterium-Tritium Layer Formation for the National Ignition Facility. *Fusion Sci. and Tech.*, **59**, 14-25 (2011).

19. Glebov, V. Yu. *et al.* Development of nuclear diagnostics for the National Ignition Facility. *Rev. Sci. Instrum.*, **77**, 10E715 (2006).

20. Bleuel, D. L. *et al.* Neutron activiation diagnostics at the National Ignition Facility. *Rev. Sci. Instrum.*, **83**, 10D313 (2012).

21. Gatu Johnson, M. *et al.* Neutron spectrometry – An essential tool for diagnosing implosions at the National Ignition Facility. *Rev. Sci. Instrum.* **83**, 10D308 (2012).

22. Spears, B. K. *Private Communication* (2013).

23. Bosch, H.-S. & Hale, G. M. Improved formulas for fusion cross-section and thermal reactivities. *Nuclear Fusion*, **32**, 611-631 (1992).

24. Krokhin, O. N. & Rozanov, V. B. Escape of α-particles from a laser-pulse-initiated thermonuclear reaction. *Soviet J. of Quantum Electronics*, **2**, 393-394 (1973).

25. Atzeni, S. & Meyer-ter-Vehn, J. *The Physics of Inertial Fusion*, 398 and 32, (Oxford University Press, 2004).

26. Patel, P. *et al.* Performance of DT layered implosions on the NIF (NO4 1), *Bull. of the American Phys. Soc. 55th Annual Meeting of the APS Division of Plasma Physics*, **58**, 193 (2013).

27. Cerjan, C., Springer, P. T. & Sepke, S. M. Integrated diagnostic analysis of inertial confinement fusion capsule performance. Phys. Plasmas, **20**, 056319 (2013).

28. Zimmerman, G. B. & Kruer, W. L. Numerical Simulation of laser initiated fusion. *Comments Plasma Phys. Controlled Fusion*, **2**, 85-89 (1975).

29. Betti, R. *et al.* Thermonuclear ignition in inertial confinement fusion and comparison with magnetic confinement. *Phys. Plasmas*, **17**, 058102 (2010).

30. Goncharov, V. N. *et al.* Improved Performance of Direct-Drive ICF Target Designs with Adiabat Shaping Using an Intense Picket. *Phys. Plasmas*, **10**, 1906-1918 (2003).

Methods

Hot-spot volume formulea. Using Eq. (2) the volume is $V_{hs} = 2\pi \int_0^\pi \int_0^{R_{hs}(\theta)} R^2 dR \sin\theta d\theta = \frac{4}{3}\pi P0^3 + \frac{4}{5}\pi P0P2^2 + \frac{8}{105}\pi P2^3 + \frac{4}{7}\pi P0P3^2 + \frac{16}{105}\pi P2P3^2 + \frac{4}{9}\pi P0P4^2 + \frac{8}{35}\pi P2^2P4 + \frac{80}{693}\pi P2P4^2 + \frac{8}{77}\pi P3^2P4 + \frac{24}{1001}\pi P4^3 + \cdots$. A simple correction to this volume can be applied (multiply) to include m-modes (azimuthal modes): $1 + \frac{3}{2}\left(\frac{M2}{M0}\right)^2 + \frac{3}{2}\left(\frac{M3}{M0}\right)^2 + \frac{3}{2}\left(\frac{M4}{M0}\right)^2 + \frac{3}{3}\frac{M2^2M4}{M0^3}\cos[4*(\phi_2 - \phi_4)]\cdots$, where ϕ_2 and ϕ_4 are phase offsets of m-modes 2 and 4 respectively.

DT reaction-rate formulea. From Bosch and Hale[23]

$$\langle\sigma v\rangle = C_1\zeta^{-5/6}\xi^2\exp\left(-3\zeta^{1/3}\xi\right) \tag{9}$$

in cm^3/s where

$$\xi = \frac{C_0}{T_{ion}^{1/3}}; \ \zeta = 1 - \frac{C_2 T_{ion} + C_4 T_{ion}^2 + C_6 T_{ion}^3}{1 + C_3 T_{ion} + C_5 T_{ion}^2 + C_7 T_{ion}^3} \tag{10}$$

and $C_0 = 6.6610$, $C_1 = 6.4341 \times 10^{-14}$, $C_2 = 1.5136 \times 10^{-2}$, $C_3 = 7.5189 \times 10^{-2}$, $C_4 = 4.6064 \times 10^{-3}$, $C_5 = 1.35 \times 10^{-2}$, $C_6 = -1.0675 \times 10^{-4}$, $C_7 = 1.366 \times 10^{-5}$ when T_{ion} is in keV units.

DT Fuel Density Profile. Assuming a density profile changes the form of Eq. (6) slightly, but the numerical value for the fuel thickness little. For example, assuming a top-hat distribution for the fuel yields $r_{out} - r_{hs} = \frac{1}{2}\sqrt{(3m_{fuel})/(\pi(\rho r)_{fuel}) - 3r_{hs}^2} - 3r_{hs}/2$ from which on obtains $r_{out} - r_{inner} = 15.5$ - 16.2 μm for N130927. The fuel density does show more sensitivity, being $\rho_{fuel} = (\rho r)_{fuel}/(r_{out} - r_{in}) = 457$ - 478 g/cc for a top-hat distribution and $\rho_{fuel} = (\rho r)_{fuel}/(\sqrt{2\pi}\sigma) = 385$ - 402 for a Gaussian. The Gaussian profile assumption is more consistent with simulated fuel density profiles. The lower fuel density associated with the Gaussian profile assumption increases the inferred fuel adiabat and decreases the fuel optical depth as compared to the uniform profile assumption. The lower fuel optical depth makes the x-ray energy contribution to Eq. (8) larger, i.e. gives us a more conservative contribution to the total DT energy.

Neutron image shape analysis. For N130927 the Legendre mode shape coefficients for the down-scattered neutron image are $P0 = 55 \pm 4$ μm, $P2/P0 = 1 \pm 5\%$, $P4/P0 = -2\%$ and for the direct image $P0 = 32 \pm 4$ μm, $P2/P0 = -35 \pm 5\%$, $P4/P0 = 2\%$. For the N131119 down-scattered neutron image $P0 = 50 \pm 4$ μm, $P2/P0 = 0 \pm 5\%$, $P4/P0 = 2\%$ and for the direct image $P0 = 34 \pm 4$ μm, $P2/P0 = -34 \pm 5\%$, $P4/P0 = 1\%$.

Author Contributions O.A.H. was lead scientist for the High-foot Campaign, performed 2D stability modeling, and 1D pre- and post-shot analysis. D.A.C. was lead scientist on shape/hohlraum strategies. D.T.C. was part of the DT shot experiment team. P.M.C. performed VISAR data unfolds. C.C. performed 3D "detailed model" calculations. E.L.D. was lead experimenter for 1DConA (R(t) trajectory) tuning experiments and capsule re-emission (early-time symmetry) tuning experiments. T.R.D. performed initial 1D capsule design, scoping, and 1D pre- and post- shot simulations. T.D. was lead experimentalist on a 2DConA ablator shape experiment and was part of the DT shot team. D.E.H. was the pulse-shape design physicist and performed all 2D integrated hohlraum-capsule simulations. L.F.B.H. was design physicist for keyhole (shock-timing) tuning experiments. J.L.K. was lead experimentalist for symcap (hot-spot shape) tuning experiments. S.L. was lead experimentalists for the keyhole (shock-timing) experiments. T.M. was lead experimentalist for several 2DConA ablator shape experiments, was part of the DT shot team, and lead on shot N131119. A.G.M. was part of the 1DConA and DT experiment teams. J.L.M. was re-emission

experiment design physicist. A.P. was part of the DT shot team. P.K.P. provided a hot-spot model analysis and metrics plots. H.-S. P. was lead experimentalist on DT implosion shots up to and including N130927. B.A.R. was overall lead on experiments. J.D.S. constructed model multi-frequency sources normalized to tuning experiments and performed 1D and 2D model scoping. P.T.S. provided a hot-spot model analysis. R.T. provided 1DConA analysis and was shot experimentalist.

Competing Interests   The authors declare that they have no competing financial interests.

Correspondence   Correspondence and requests for materials should be addressed to O.A.H. (email: hurricane1@llnl.gov).

Table 1: Table of measured and derived implosion performance metrics. Lines 1-9 for columns 2-3 are directly measured quantities, others are derived from the data. Columns 4, 5 and 6 show results from two data driven models and simulation, respectively.
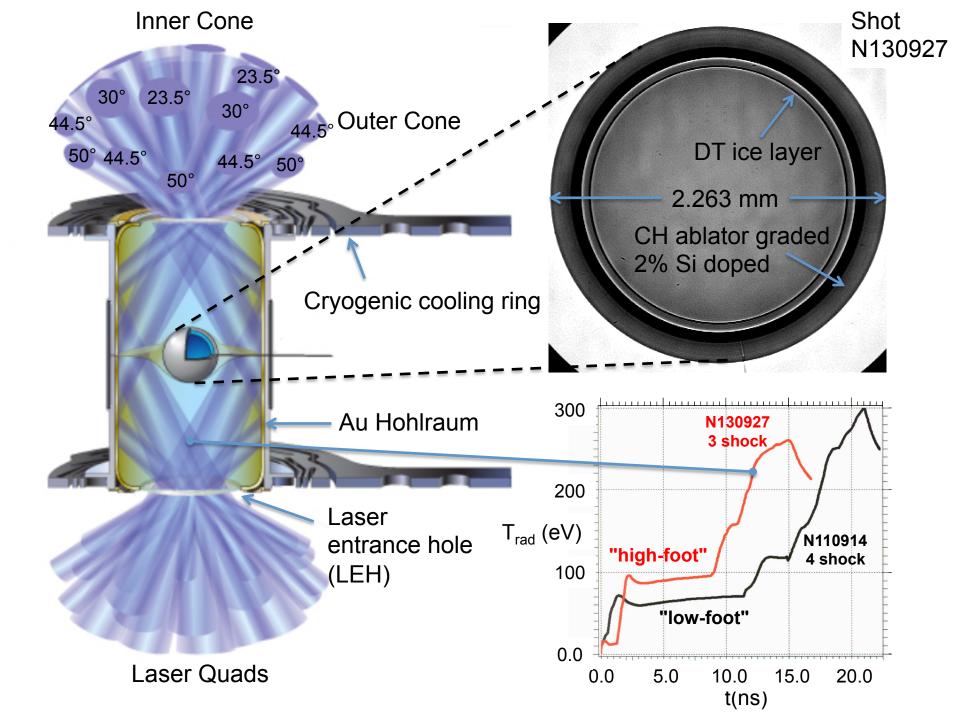
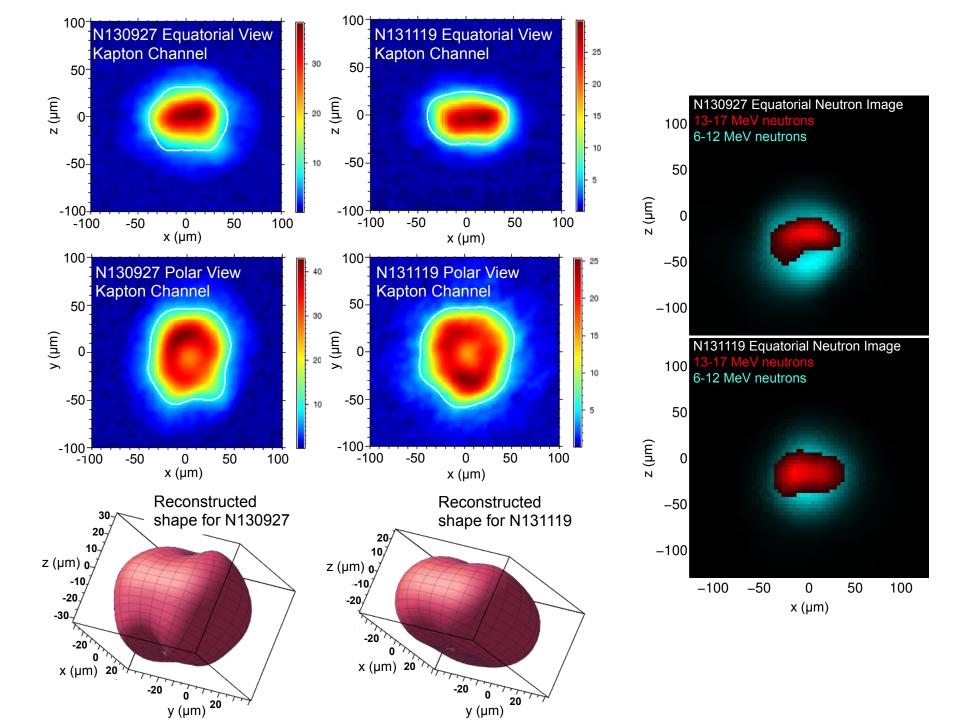| Quantity	N131119$_{1.9\ MJ}^{425\ TW}$	N130927$_{1.8\ MJ}^{390\ TW}$	P.P.[26]$_{N130927}$	P.T.S.[27]$_{N130927}$	Sim.$_{N130927}$
Y_{13-15} (neut.'s)	$5.2 \pm 0.097 \times 10^{15}$	$4.4 \pm 0.11 \times 10^{15}$	–	–	7.6×10^{15}
T_{ion} (keV) DT	5.0 ± 0.2	4.63 ± 0.31	–	–	4.2
T_{ion} (keV) DD	4.3 ± 0.2	3.77 ± 0.2	–	–	3.9
DSR (%)	4.0 ± 0.4	3.85 ± 0.41	–	–	4.1
τ_x (ps)	152.0 ± 33.0	161.0 ± 33.0	–	–	137
$P0_x$, $P0_n$ (μm)	$35.8 \pm 1.0, 34 \pm 4$	$35.3 \pm 1.1, 32 \pm 4$	–	–	32
$P2/P0_x$	-0.34 ± 0.039	-0.143 ± 0.044	–	–	–
$P3/P0_x$	0.015 ± 0.027	-0.004 ± 0.023	–	–	–
$P4/P0_x$	-0.009 ± 0.039	-0.05 ± 0.023	–	–	–
Y_{total} (neut.'s)	6.1×10^{15}	5.1×10^{15}	–	–	8.9×10^{15}
E_{fusion} (kJ)	17.3	14.4	–	–	25.1
r_{hs} (μm)	36.6	35.5	$34.4 - 42.3$	$35.7 - 36.0$	32.2
$(\rho r)_{hs}$ (g/cm^2)	$0.12 - 0.15$	$0.12 - 0.18$	$0.13 - 0.19$	$0.1 - 0.14$	0.15
E_{hs} (kJ)	$3.9 - 4.4$	$3.5 - 4.2$	$3.7 - 5.5$	$3.71 - 4.56$	4.1
E_α (kJ)	$2.2 - 2.6$	$2.0 - 2.4$	$2.0 - 2.4$	$2.0 - 2.5$	2.8
$E_{DT,total}$ (kJ)	$8.5 - 9.4$	$10.2 - 12.0$	$10.0 - 13.9$	$10.92 - 11.19$	13.4
G_{fuel}	**$1.8 - 2.0$**	**$1.2 - 1.4$**	**$1.04 - 1.44$**	**$1.28 - 1.31$**	**1.9**

Figure 1 **Indirect Drive ICF target for NIF**. A schematic NIF ignition target shows a cut-away of the gold hohlraum and plastic capsule with representative laser bundles incident on the inside surface of the hohlraum on the left frame. An x-ray image of the actual capsule for N130927 with DT fuel layer is shown with dimension noted in the upper right and the x-ray radiation drive temperature vs. time for the NIC low-foot implosion and post-NIC high-foot implosion is shown on the lower right.
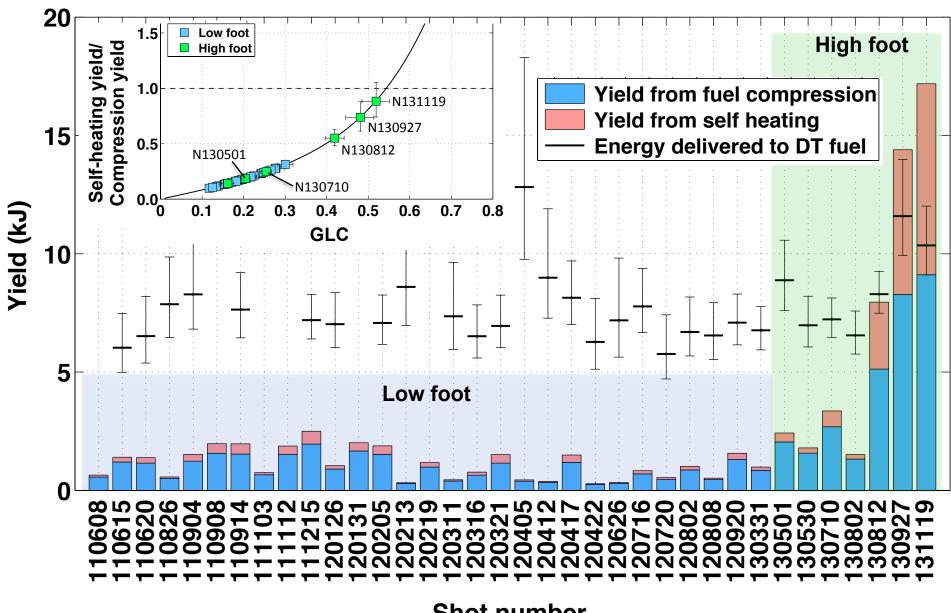
Figure 2 **X-ray and neutron images of the hot-spot at bang-time**. The left column shows the hot-spot shape for N130927 from the equatorial (side-on) and polar (top down) view. The center column shows the hot-spot shape for N131119. 3D reconstructions of the hot-spot are shown on the bottom of the figure. In the x-ray images, the contour shown in white is taken at the 17% peak brightness level and is used to obtain a the description of the shape in Legendre modes (equatorial view) and Fourier modes (polar view). On the right side, is shown a superposition of direct (13-17 MeV) and down-scatter (6 - 12 MeV) neutron images from N130927 and N131119. (X-ray image analysis courtesy of N. Izumi, S. Khan, T. Ma, and A. Pak of the NIF Shape Working Group and neutron image analysis courtesy of D. Fittinghoff, G. Grim, N. Guler, and F. Merrill of the NIF Neutron Imaging System Working Group.)

Figure 3 **Yield and energetics metrics for shots on the NIF.** Total fusion yield is plotted versus shot number (i.e. time). Shots 110608-130331 are low-foot shots. Shots 130501-131119 are high-foot shots. The bars showing total yield are broken into components of

yield coming from α-particle self-heating and yield coming from compression. The black dashes denote the energy delivered to the DT (fuel + hot-spot) with error bars (black vertical lines, formal $\pm1\sigma$ standard deviations) as calculated from the P.P.[26] model. The plot shows that, outside of error bars, shots 130927 and 131119 both yielded more fusion energy than was delivered to the DT. The insert shows the ratio of self-heating yield divided by compression yield versus generalized Lawson criteria with error bars (formal $\pm1\sigma$ standard deviations) on the yield ratio and GLC.

Inner Cone

23.5°
30° 23.5°
30°
44.5° 44.5°
50° 44.5° 44.5° 50°
50° 50°

Outer Cone

Cryogenic cooling ring

Au Hohlraum

Laser entrance hole (LEH)

Laser Quads

DT ice layer

2.263 mm

CH ablator graded 2% Si doped

T_{rad} (eV)

N130927 3 shock

"high-foot"

"low-foot"

N110914 4 shock

t(ns)

N130927 Equatorial View Kapton Channel

N131119 Equatorial View Kapton Channel

N130927 Polar View Kapton Channel

N131119 Polar View Kapton Channel

Reconstructed shape for N130927

Reconstructed shape for N131119

N130927 Equatorial Neutron Image
13-17 MeV neutrons
6-12 MeV neutrons

N131119 Equatorial Neutron Image
13-17 MeV neutrons
6-12 MeV neutrons